Dalton Transactions

Unusual aliovalent doping effects on oxygen non-stoichiometry in medium-entropy compositionally complex perovskite oxides

Journal:	*Dalton Transactions*
Manuscript ID	DT-ART-11-2022-003759.R1
Article Type:	Paper
Date Submitted by the Author:	18-Dec-2022
Complete List of Authors:	Zhang, Dawei; UC San Diego Park, Jiyun; Brown University, School of Engineering, Xu, Boyuan; Brown University, Physics Liu, Cijie; West Virginia University Li, Wei; West Virginia University College of Engineering and Mineral Resources, Department of Mechanical and Aerospace Engineering Liu, Xingbo; West Virginia University, Department of Mechanical and Aerospace Engineering Qi, Yue; Brown University Luo, Jian; UC San Diego,

Unusual aliovalent doping effects on oxygen non-stoichiometry in medium-entropy compositionally complex perovskite oxides

Dawei Zhang,[a] Jiyun Park,[b,] Boyuan Xu,[c] Cijie Liu,[d] Wei Li,[d] Xingbo Liu,[d] Yue Qi,[b] and Jian Luo [a,e,#]

[a] Program of Materials Science and Engineering, University of California San Diego, La Jolla, CA, 92093, USA

[b] School of Engineering, Brown University, Providence, Rhode Island 02912, USA

[c] Department of Physics, Brown University, Providence, Rhode Island 02912, USA

[d] Department of Mechanical and Aerospace Engineering, Benjamin M. Statler College of Engineering and Mineral Resources, West Virginia University, Morgantown, WV 26506, USA

[e] Department of NanoEngineering, University of California San Diego, La Jolla, CA, 92093, USA

Abstract

Aliovalent doping on perovskite oxides can tune the oxygen vacancy formation energy. This work discovers normal *vs.* abnormal aliovalent doping effects on redox behaviors in medium-entropy compositionally complex perovskite oxides (CCPOs) $(La_{1-x}Sr_x)(Mn_{1/3}Fe_{1/3}Ti_{1/3})O_{3-\delta}$ (LS_MFT) *vs.* $(La_{1-x}Sr_x)(Mn_{1/3}Fe_{1/3}Cr_{1/3})O_{3-\delta}$ (LS_MFC). In the LS_MFC series, oxygen non-stoichiometry range $\Delta\delta$ ($= \delta_{red} - \delta_{ox}$) linearly depends on the Sr molar ratio x, while the LS_MFT series shows a V-shape dependence of $\Delta\delta$ on x. This unusual observation is investigated and explained based on the analysis of energy loss near edge structure (ELNES) in STEM electron energy loss spectroscopy, along with density functional theory (DFT) calculations. In LS_MFC, Cr-$L_{2,3}$, Mn-$L_{2,3}$ and Fe-$L_{2,3}$ peaks have a similar linear shift to higher energy with increasing x, which indicates higher oxidation states of Cr, Mn, and Fe with lower oxygen vacancy formation energies. In LS_MFT, the V-shape of $\Delta\delta$ *vs.* x curve is caused by the stable Ti^{4+} state and a V-shape Mn/Fe valency dependence on x. This study suggests the possible existence of different (including unexpected) coupled aliovalent doping effects in CCPOs with multiple B-site redox active elements.

[#] Corresponding Author: jluo@alum.mit.edu

1. Introduction

Non-stoichiometric $ABO_{3-\delta}$ perovskite oxides have been proposed and explored as competitive candidates for several energy related applications, including solar thermochemical renewable fuel production,[1–4] ferroelectric materials,[5–7] and energy conversion devices.[8–10] The oxygen vacancies in $ABO_{3-\delta}$ facilitates oxygen reduction reactions.[11–13] Tailoring the oxygen non-stoichiometry by aliovalent doping has been proven to be an effective way to tailor the properties of perovskite oxides. For instance, doping $LaMnO_3$ and $LaFeO_3$ with 2+ alkaline earth elements like Sr and Ba can reduce the enthalpies of oxygen vacancy formation.[14,15] The substitution of La^{3+} with 2+ cations can introduce extra holes to the perovskite oxides, which increase the B-site metal cation oxidation states.[16,17] Similarly, B-site doping can create mixed valence states and tune the thermodynamic properties of perovskite oxides. Qian *et al*.[4] reported that Ti substitution of Mn in $Ca(Mn_{0.5}Ti_{0.5})O_3$ resulted in a significant improvement of H_2 generation in thermochemical cycling. In addition, simultaneous doping both A- and B-sites can further tune the properties of perovskite oxides.[18,19] A recent high-throughput study of the oxygen chemical potential engineering of perovskite oxides via machine learning also suggested improved redox properties of perovskite with multiple cations on both A- and B-sites.[20]

The emergent high-entropy ceramics (HECs),[21–24] as well as a broader class of compositionally complex ceramics (CCCs),[2,25] with multiple primary elements on A- and/or B-site cation sublattices offer a new opportunity to search for redox materials with a vast and tunable compositional space. With the increasing number of primary elements on the cation sublattices, the aliovalent doping effects can become complicated, producing new phenomena of potential scientific and technological interests. To date, the redox mechanisms in perovskite oxides with multiple redox active elements on the B site, as well as how they may interact with A-site doping, remain elusive, which motivated this study.

In this study, we synthesized two series of medium-entropy compositionally complex perovskite oxides (CCPOs) $(La_{1-x}Sr_x)(Mn_{1/3}Fe_{1/3}Cr_{1/3})O_3$ (denoted as "LS_MFC") and $(La_{1-x}Sr_x)(Mn_{1/3}Fe_{1/3}Ti_{1/3})O_3$ (denoted as "LS_MFT"), where we changed Sr molar ratio (x) on the A site and investigated the oxygen non-stoichiometry under thermochemical cycles. We discovered normal vs. abnormal behaviors in the reversible extent of reduction ($\Delta\delta$) *vs.* Sr molar ratio relations in LS_MFC (linear) and LS_MFT (V-

shape). Combining the analysis of energy loss near edge structure (ELNES) in the electron energy loss spectra (EELS) in aberration-corrected scanning transmission electron microscopy (AC STEM) with density functional theory (DFT) calculations, we showed that the replacement of Ti with Cr alters the effect of Sr dopant due to the stable Ti^{4+} state. This new finding suggests that the simultaneous doping on A and B sites can have coupling effects, which can lead to both complexity and opportunities to tailor compositionally complex oxides with three or more primary redox active cations on one sublattice.

2. Results and discussions

All CCPO specimens were synthesized by a conventional solid-state method described in Electronic Supplemental Information (ESI†). The specific compositions and abbreviations are listed in Table 1.

Table 1. A list of 10 compositions of the samples investigated in this study and their abbreviations.

Sample Abbreviation	Sample Composition
L_MFT	$La(Mn_{1/3}Fe_{1/3}Ti_{1/3})O_3$
LS82_MFT	$(La_{0.8}Sr_{0.2})(Mn_{1/3}Fe_{1/3}Ti_{1/3})O_3$
LS55_MFT	$(La_{0.5}Sr_{0.5})(Mn_{1/3}Fe_{1/3}Ti_{1/3})O_3$
LS46_MFT	$(La_{0.4}Sr_{0.6})(Mn_{1/3}Fe_{1/3}Ti_{1/3})O_3$
LS28_MFT	$(La_{0.2}Sr_{0.8})(Mn_{1/3}Fe_{1/3}Ti_{1/3})O_3$
S_MFT	$Sr(Mn_{1/3}Fe_{1/3}Ti_{1/3})O_3$
L_MFC	$La(Mn_{1/3}Fe_{1/3}Cr_{1/3})O_3$
LS55_MFC	$(La_{0.5}Sr_{0.5})(Mn_{1/3}Fe_{1/3}Cr_{1/3})O_3$
LS37_MFC	$(La_{0.3}Sr_{0.7})(Mn_{1/3}Fe_{1/3}Cr_{1/3})O_3$
S_MFC	$Sr(Mn_{1/3}Fe_{1/3}Cr_{1/3})O_3$

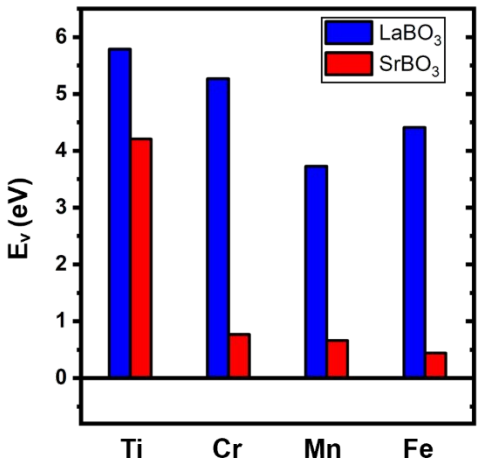

Fig. 1 DFT-calculated oxygen vacancy formation energies of all possible element combinations of ternary perovskite oxides $LaBO_3$ and $SrBO_3$ (B = Ti, Cr, Mn, or Fe).

Fig. 1 displays the oxygen vacancy formation energy (E_v^f) of eight ternary perovskites with random combinations of elements in LS_MFT and LS_MFC calculated by density functional theory (DFT). The details of the calculations can be found in the ESI†. The blue and red bars represent DFT-calculated results for the $LaBO_3$ and $SrBO_3$ structures, respectively. In general, for a specific B-site element, $SrBO_3$ exhibits a lower oxygen vacancy formation energy than $LaBO_3$. Ternary perovskites with Ti on the B site maintain a higher oxygen vacancy formation energy ($LaTiO_3$ 5.79 eV, $SrTiO_3$ 4.21 eV) compared to other ternary perovskites. In addition, we notice that $LaTiO_3$ and $SrTiO_3$ have smaller differences on oxygen vacancy formation energies in contrast to the much larger differences present in Cr, Mn and Fe contained ternary perovskites. One reason for this phenomenon is due to the empty *d* orbital structure ($3d^0$) of Ti^{4+}. Even though the Sr substitution increases the oxidation state of Ti, the stable $3d^0$ valence structure also effectively prevents the Ti reduction and oxygen vacancy formation in $SrTiO_3$. Similarly, $LaFeO_3$ (4.41 eV) and $SrFeO_3$ (0.44 eV) have a large difference in oxygen vacancy formation energy because the half-filled $3d^5$ structure in Fe^{3+} allows much lower energy barriers of the Fe^{4+} to Fe^{3+} reduction, in comparison with that of Fe^{3+} to Fe^{2+}.

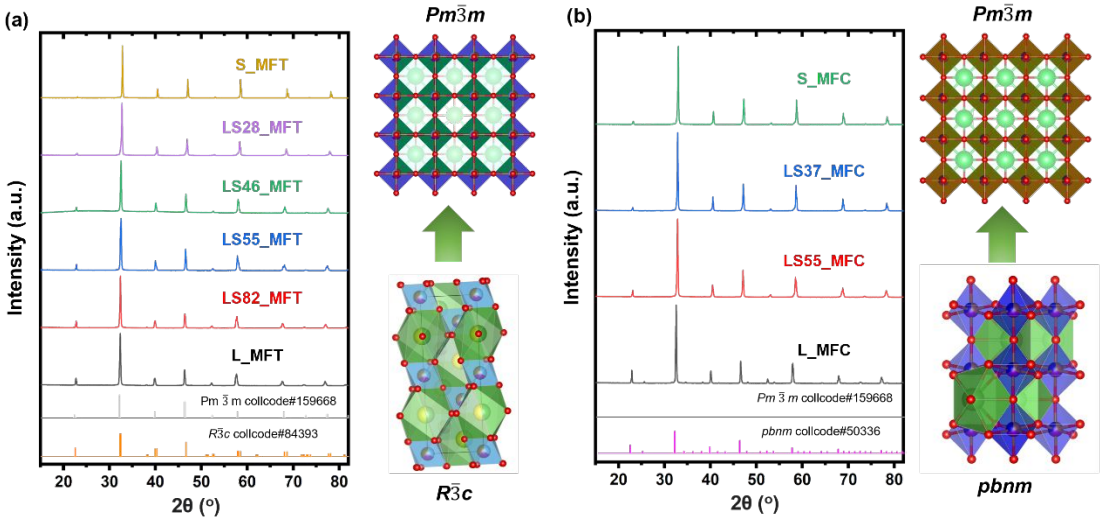

Fig. 2 XRD patterns of the (a) synthesized LS_MFT series with a gradual transition from the rhombohedral $R\bar{3}c$ (L_MFT) to cubic $Pm\bar{3}m$ (S_MFT) structure and (b) synthesized LS_MFC series with a gradual transition from orthorhombic *pbnm* (L_MFC) to cubic $Pm\bar{3}m$ (S_MFC) structure. See Fig. S1† for enlarged views of the XRD patterns of the (113) peak area to show this phase transition clearly.

Fig. 2a and 2b display the XRD patterns of the LS_MFT and LS_MFC series, respectively. From L_MFT to LS46_MFT, the XRD patterns can be indexed with a rhombohedral $R\bar{3}c$ structure (ICSD collcode #84393). Higher Sr doping on the A site (with a larger A site ionic radius) leads to a structural transition to a cubic $Pm\bar{3}m$ structure (ICSD collcode #159668) in LS28_MFT and S_MFT. The phase transition from rhombohedral to cubic structure was clearly evident by the evolution of peak (113) at around 38º shown in Fig. S1†. In the LS_MFT series, the rhombohedral (R$\bar{3}$c) to cubic (Pm$\bar{3}$m) phase transition from is mainly controlled by the Goldschmidt tolerance factor, $t = (r_A + r_O)/[\sqrt{2}(r_B + r_O)]$, where r_A, $r_B$and r_O, respectively, are the ionic radiii of A- and B-site cations and O anions, respectively. The rhombohedral-to-cubic phase transformation takes place at around t = 1, as shown in the new Fig. S7 (also shown below). In the LS_MFC series, L_MFC exhibited an orthorhombic *pbnm* structure (ICSD collcode #50336). The other three compositions showed the cubic $Pm\bar{3}m$ structure. To further examine the elemental homogeneity of these samples, we conducted high-resolution scanning electron microscopy SEM) energy dispersive X-ray spectroscopy (EDS) mapping. The SEM images and EDS elemental maps were shown in Fig. S2† (LS_MFT) and S3† (LS_MFC). Most LS_MFT specimens maintain homogenous elemental distributions (except that LS82_MFT shows some minor La inhomogeneity). LS_MFC specimens show mostly uniform distribution albeit minor Cr enriched areas.

The redox capabilities were quantified by temperature programmed reduction (TPR) in thermogravimetric analysis (TGA) for all LS_MFT (for six different compositions) and LS_MFC (for four different compositions) by measuring Δδ, as shown in Fig. 3a (LS_MFC) and 3b (LS_MFT). In thermochemical reactions (*e.g.*, solar thermochemical hydrogen production), perovskite oxides undergo the cycling between reduced ($ABO_{3-\delta red}$) and oxidized ($ABO_{3-\delta ox}$) states and Δδ (= $\delta_{red} - \delta_{ox}$) measures the intrinsic amount of oxygen non-stoichiometry can be applied to generate renewable fuels such as H_2 (albeit at different specific P_{O2} conditions). For all TPR measurements, two consecutive redox cycles were performed with 45 min reduction at 1350 ºC under Ar and 25 min oxidation at 900 ºC under 21% O_2 balanced with Ar. The mass loss of the first cycle usually contains volatilization of surface absorbates like H_2O and amorphous carbon. Hence, the second cycles were reported here. The plateau of the oxidation step (21% O_2) of the first cycle was set as the zero reference to compare the oxygen non-stoichiometry (Δδ) of different compositions. The temperature profile is presented as the dash line in the same figure.

Fig. 3c and 3d show the quantified Δδ *vs.* Sr molar ratio on the A site of LS_MFC and LS_MFT, respectively. The Δδ of LS_MFC exhibits an expected (normal) linear increasing trend with the Sr molar

ratio on the A site. The linear trend is similar to those the widely reported compositions like (La,Sr)MnO_3,[1,18] corresponding to the increase of oxidation state of B site elements with Sr substitution of La on the A site.

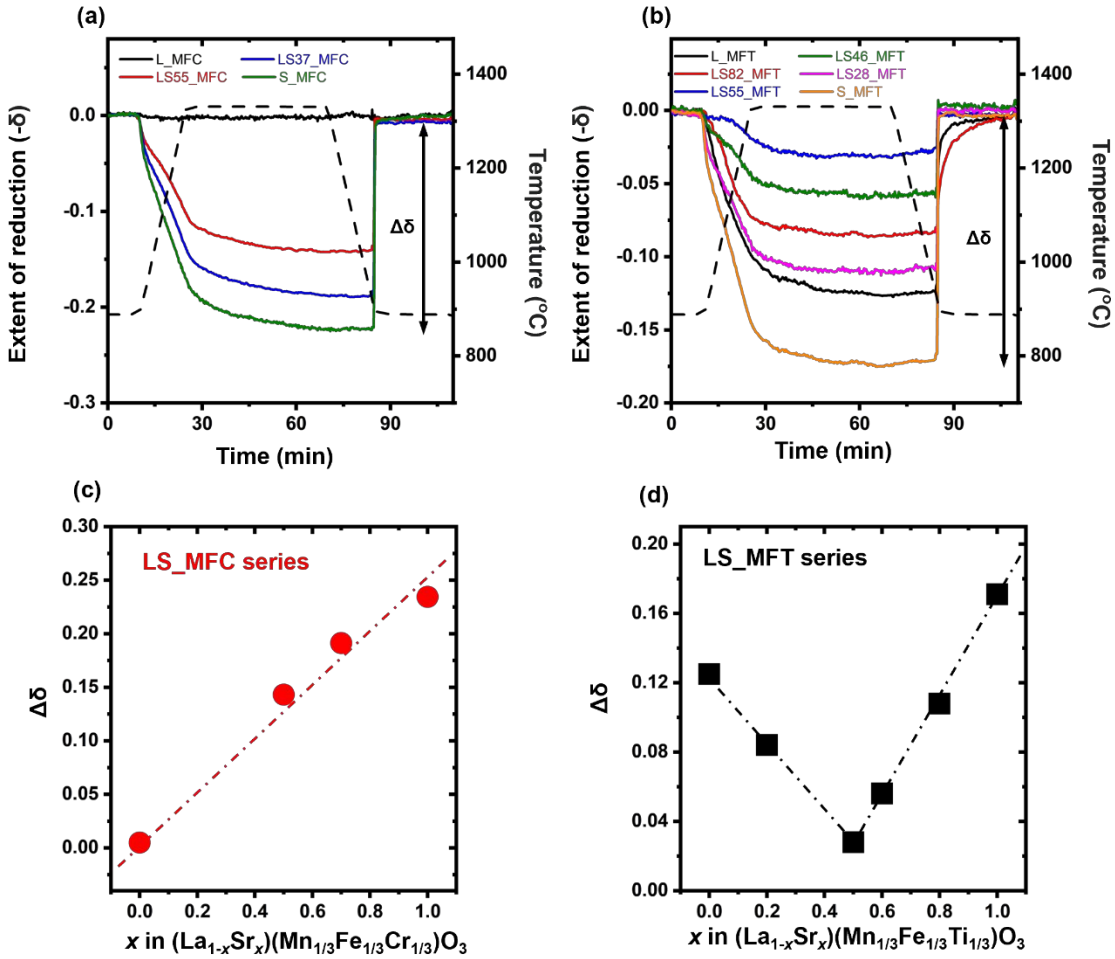

Fig. 3 Temperature programed reduction measurements of the (a) LS_MFC and (b) LS_MFT series. The reduction was conducted at 1350 °C for 45 min under Ar and the oxidation was conducted at 900 °C for 25 min under 21% O_2 balanced with Ar. The measurements contained two consecutive cycles and the second cycles were shown here (to exclude effects from volatile surface absorbates in the first cycle). The reference was calibrated to the oxidization state at the beginning of the second cycle. The calculated Δδ *vs. x* curves are shown in (c) for $(La_{1-x}Sr_x)(Mn_{1/3}Fe_{1/3}Cr_{1/3})O_3$ (LS_MFC) and in (d) for $(La_{1-x}Sr_x)(Mn_{1/3}Fe_{1/3}Ti_{1/3})O_3$ (LS_MFT) series, respectively. Noting that the δ values measured by TGA are relative and used to determine Δδ (= $\delta_{red} - \delta_{ox}$).

Interestingly, Fig. 3d displays an abnormal V-shape relation in Δδ *vs.* Sr molar ratio curve in LS_MFT, which is markedly different from the (normal) linear trend observed in LS_MFC. The Δδ of LS_MFT first descends with Sr doping level from $x = 0$ ($\Delta\delta = 0.124$) to $x = 0.5$ ($\Delta\delta = 0.027$) on the A

site, and increases again to reach the maximum ($\Delta\delta = 0.170$) when Sr fully occupies A site. In LS_MFT, the minimum of $\Delta\delta$ (0.027) occurs in LS55_MFT (*i.e.*, $x = 0.5$), in contrast to LS_MFC that has the minimum in L_MFC (*i.e.*, $x = 0$).

The only difference between LS_MFT and LS_MFC is the replacement of Cr by Ti, which caused the Sr doping effect to change from a linear to a V-shape trend. To further confirm that the V-shape correlates with Ti, a series of $(La_{1-x}Sr_x)(Mn_{0.5}Fe_{0.5})O_3$ were tested with the same TPR protocol and formed a linear relation between $\Delta\delta$ and Sr molar ratio, as shown in Fig. S4 †. Furthermore, we investigated how the Ti doping (with unchanged valence as we show latter) can tune the chemical properties of Mn and Fe at various Sr doping levels, which represents an interesting and intriguing finding.

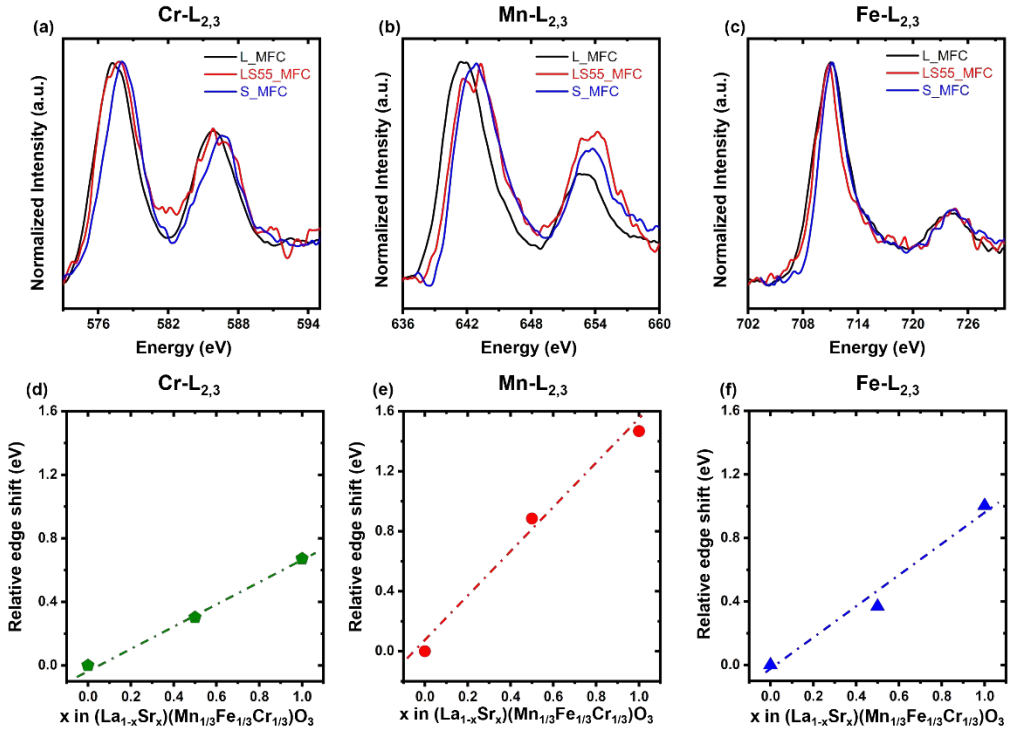

Fig. 4 Energy loss near edge structure of the (a) Cr-$L_{2,3}$, (b) Mn-$L_{2,3}$, and (c) Fe-$L_{2,3}$ in LS_MFC series. The edge onset was calibrated to the energy with 20% of the maximum for the elements. The relative edge shift was calculated with respect to the edge energy of L_MFC. The relative edge shifts of (d) Cr-$L_{2,3}$, (e) Mn-$L_{2,3}$, and (f) Fe-$L_{2,3}$ in the LS_MFC series all show a linear relation *vs.* x in $(La_{1-x}Sr_x)(Mn_{1/3}Fe_{1/3}Cr_{1/3})O_3$.

To investigate the underlying mechanism that results in the different $\Delta\delta$ *vs.* Sr molar ratio curves shown in Fig. 3c and 3d, we measured the chemical shift of B-site elements of LS_MFC and LS_MFT

by EELS under an AC STEM in high-angle annular dark-field (HAADF) imaging mode. Fig. 4 a-c show the energy loss near edge structure (ELNES) of the Cr-$L_{2,3}$, Mn-$L_{2,3}$ and Fe-$L_{2,3}$ peaks with different Sr molar ratios in the LS_MFC series. The intensities of all spectra were computed and normalized to the intensity of the highest peak (set to be 1 as the reference value). To quantify the chemical shift of specific elements, the energy loss where the edge energy reaches 20% of its peak maximum is taken as the edge onset. In general, the energy onset position of 3*d* transition metals L edge shifts to higher energy-loss position for higher valence state.[26] Fig. 4 d-f show the computed relative edge shift of the Cr-$L_{2,3}$, Mn-$L_{2,3}$, and Fe-$L_{2,3}$ peaks in the LS_MFC series, calculated by subtracting the energy edge from that of L_MFC (as the reference; relative edge shift = 0). The Cr-$L_{2,3}$, Mn-$L_{2,3}$ and Fe-$L_{2,3}$ peaks all shift linearly to higher energy with increasing Sr molar ratio, which suggests increased valence of Cr, Mn, and Fe. The increasing oxidation state of B-site elements with higher Sr molar ratio correlates well with the oxygen non-stoichiometry measurements of the LS_MFC series shown in Fig. 3c.

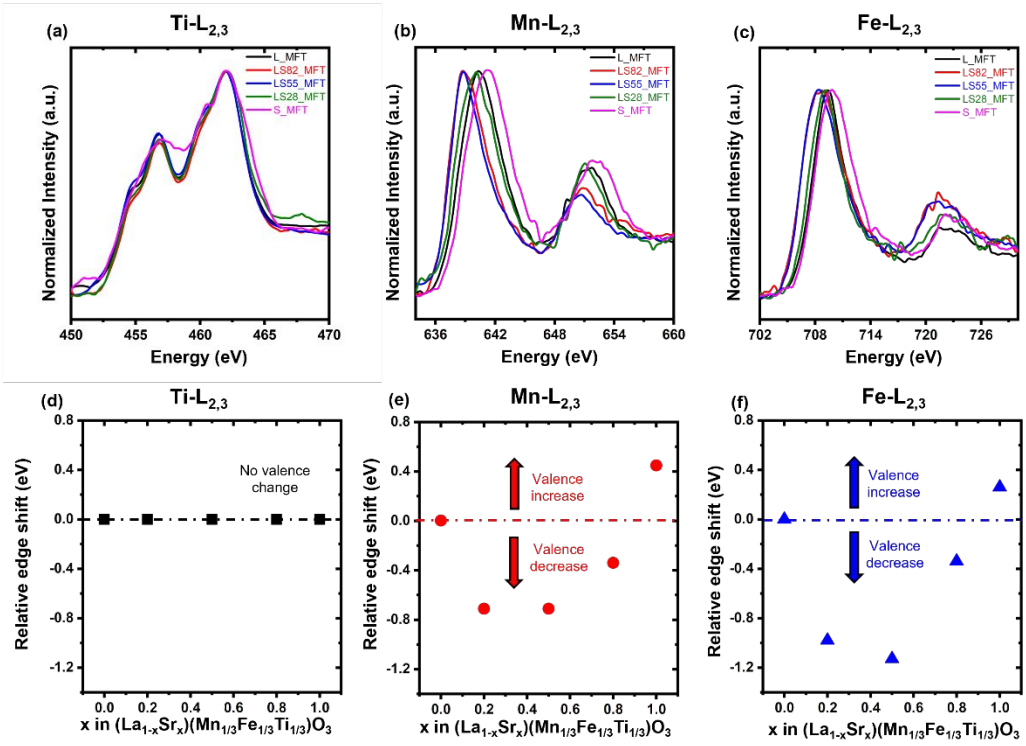

Fig. 5 Measured energy loss near edge structures of the (a) Ti-$L_{2,3}$, (b) Mn-$L_{2,3}$, (c) Fe-$L_{2,3}$ in LS_MFC series. The edge onset was calibrated to the energy with 20% of the maximum for the elements. The relative edge shifts were calculated with respect to the edge energy of the L_MFT. The relative edge shift of the (d) Ti-$L_{2,3}$ was at zero, indicating no chemical shift of Ti. (e, f) The relative edge shifts of Mn and Fe, which shows a shift to lower energy (decreasing valence state),

followed by a shift to higher energy (increasing valence state) as x in $(La_{1-x}Sr_x)(Mn_{1/3}Fe_{1/3}Ti_{1/3})O_3$ is increased.

As a comparison, Fig. 5 shows the Ti-$L_{2,3}$, Mn-$L_{2,3}$ and Fe-$L_{2,3}$ in the LS_MFT series with the calculated relative shift of the corresponding elements. The dash lines drawn in Fig. 5 d-f represent the reference state (L_MFT) for comparison. The Ti-$L_{2,3}$ peak stays at the zero-edge shift, which implies no oxidation state change of Ti regardless of the Sr molar ratio. Compared to Mn and Fe, Ti has a much higher oxygen vacancy formation energy in both $SrTiO_3$ and $LaTiO_3$, based on the DFT calculations shown in Fig. 1. Therefore, we conclude that aliovalent doping keeps Ti at 4+ charge state and Ti^{4+} does not participate in the redox reaction. Meanwhile, the relative edge shift of the Mn-$L_{2,3}$ and Fe-$L_{2,3}$ peaks maintained a parabolic shape first (x = 0 to 0.5) with an edge shift (0 to -0.4 eV) to a lower energy (oxidation) state, but then shift (-0.76 to 0.45 eV) to a higher energy (oxidation) state as from x = 0.5 to 1. The evolution of Mn and Fe in terms of the oxidation state followed the similar the V-shape behavior in the previous $\Delta\delta$ measurements shown in Fig. 3d. This suggests that the oxygen non-stoichiometry of LS_MFT is controlled by oxidation state of Mn and Fe. In LS_MFT82 and LS_MFT55, the edge onset positions of Fe and Mn were close to each other because the edge onset might be sensitive to the lowest oxidation state. Therefore, it is possible that charge states like Mn^{2+} exist in LS82_MFT and LS55_MFT.

Another important scientific question we investigated is the charge balance in the LS_MFT series. Sr doping should introduce extra holes in the perovskite structure. However, with 0 to 50% Sr molar ratios, we only observed a fixed-valence Ti and valence-decreasing Mn/Fe. Hence, there must be other components in the LS_MFT series to accommodate the extra holes from Sr doping. We suggest that the charge compensation can be accomplished by the oxygen vacancy formation. Thus, we further investigated the O K edge EELS spectra in the LS_MFT series, as shown in Fig. S5†. The vertical dash line labels the pre-peak that has been correlated to the oxygen vacancy formation in prior work.[27] The decrease in pre-peak intensity implies oxygen vacancy formation. In Fig. S5†, we can observe that the pre-peak has an obvious intensity decrease from L_MFT to LS55_MFT, followed by an increase from LS55_MFT to S_MFT. This finding indicates that oxygen vacancy formation in LS55_MFT and the oxygen vacancy participated in the charge compensation of Mn and Fe with decreasing oxidation state. We also applied a similar method to quantify the relative shift of O K shown in Fig. S6†. Here, we

noticed that the relation of O K edge shift with the Sr molar ratio also shows a volcan like shape. The increasing Sr doping from 0 to 50% resulted in a +0.5 eV increase in the relative energy shift in O K edge, which can be correlated with the energy shift of Mn and Fe to lower energy direction.

3. Conclusions

We discovered normal *vs.* abnormal Sr doping effects on oxygen non-stoichiometry (Δδ) in two series of medium-entropy CCPOs or compositionally complex perovskite oxides with three potentially redox active elements on the B site at equimolar fractions. The crystal structure depends on the La/Sr ratio on the A site, and it can vary from rhombohedral/orthorhombic to cubic. In the LS_MFC series with Mn, Fe and Cr on the B site, the Δδ exhibited a (normal) linear increasing relation with increasing Sr molar ratio on the A site. The linear relation between Δδ and Sr molar ratio was caused by the higher oxidation states of B site elements as verified directly in EELS measurements. In the LS_MFT series with Mn, Fe and Ti on the B site, the Δδ exhibited an abnormal V-shape correlation with the Sr molar ratio, which follows the oxidation state evolution of Mn and Fe that also shows a V-shape dependence on the Sr molar ratio.

This study exemplifies that the coupling of A- and B-site doping effects in the emerging class of compositionally complex perovskite oxides can result in unexpected phenomena. Understanding of the complex interplays of multiple redox active elements on the B site, interacting with aliovalent doping on the A site, can provide new opportunities and strategies to search and tailor new redox active compositionally complex oxides for thermochemical looping.

Acknowledgement

This work is supported by the U.S. Department of Energy (DOE), Office of Energy Efficiency and Renewable Energy (EERE), under the Agreement Number DE-EE0008839, managed by the Hydrogen and Fuel Cell Technologies Office in the Fiscal Year 2019 H2@SCALE program.

References:

1 A. H. McDaniel, E. C. Miller, D. Arifin, A. Ambrosini, E. N. Coker, R. O'Hayre, W. C. Chueh and J. Tong, *Energy Environ. Sci.*, 2013, **6**, 2424–2428.

2 S. Zhai, J. Rojas, N. Ahlborg, K. Lim, M. F. Toney, H. Jin, W. C. Chueh and A. Majumdar, *Energy Environ. Sci.*, 2018, **11**, 2172–2178.

3 R. D. Barcellos, M. D. Sanders, J. Tong, A. H. McDaniel and R. P. O'Hayre, *Energy Environ. Sci.*, 2018, **11**, 3256–3265.

4 X. Qian, J. He, E. Mastronardo, B. Baldassarri, W. Yuan, C. Wolverton and S. M. Haile, *Matter*, 2021, **4**, 688–708.

5 F. Rubio-Marcos, A. Del Campo, P. Marchet and J. F. Fernández, *Nat. Commun.*, 2015, **6**, 6594.

6 N. Horchidan, A. C. Ianculescu, C. A. Vasilescu, M. Deluca, V. Musteata, H. Ursic, R. Frunza, B. Malic and L. Mitoseriu, *J. Eur. Ceram. Soc.*, 2014, **34**, 3661–3674.

7 L. L. Zhang and Y. N. Huang, *Sci. Rep.*, 2020, **10**, 1–18.

8 Z. Shao and S. M. Haile, *Nature*, 2004, **431**, 170–173.

9 N. Tsvetkov, Q. Lu, L. Sun, E. J. Crumlin and B. Yildiz, *Nat. Mater.*, 2016, **15**, 1010–1016.

10 Y. Chen, Y. Chen, D. Ding, Y. Ding, Y. Choi, L. Zhang, S. Yoo, D. Chen, B. deGlee, H. Xu, Q. Lu, B. Zhao, G. Vardar, J. Wang, H. Bluhm, E. J. Crumlin, C. Yang, J. Liu, B. Yildiz and M. Liu, *Energy Environ. Sci.*, 2017, **10**, 964–971.

11 D. Lee, R. Jacobs, Y. Jee, A. Seo, C. Sohn, A. V. Ievlev, O. S. Ovchinnikova, K. Huang, D. Morgan and H. N. Lee, *J. Phys. Chem. C*, 2017, **121**, 25651–25658.

12 A. Jun, J. Kim, J. Shin and G. Kim, *ChemElectroChem*, 2016, **3**, 511–530.

13 Y. Li, R. Gemmen and X. Liu, *J. Power Sources*, 2010, **195**, 3345–3358.

14 M. J. Ignatowich, A. H. Bork, T. C. Davenport, J. L. M. Rupp, C. K. Yang, Y. Yamazaki and S. M. Haile, *MRS Commun.*, 2017, **7**, 873–878.

15 J. R. Scheffe, D. Weibel and A. Steinfeld, *Energy and Fuels*, 2013, **27**, 4250–4257.

16 F. Bridges, C. H. Booth, M. Anderson, G. H. Kwei, J. J. Neumeier, J. Snyder, J. Mitchell, J. S. Gardner and E. Brosha, *Phys. Rev. B - Condens. Matter Mater. Phys.*, 2001, **63**, 214405.

17 Z. L. Wang, J. S. Yin, Y. D. Jiang and J. Zhang, *Appl. Phys. Lett.*, 1997, **70**, 3362–3364.

18 Z. Chen, Q. Jiang, F. Cheng, J. Tong, M. Yang, Z. Jiang and C. Li, *J. Mater. Chem. A*, 2019, **7**, 6099–6112.

19 G. S. Gautam, E. B. Stechel and E. A. Carter, *Chem. Mater.*, 2020, **32**, 9964–9982.

20 X. Wang, Y. Gao, E. Krzystowczyk, S. Iftikhar, J. Dou, R. Cai, H. Wang, C. Ruan, S. Ye and F. Li, *Energy Environ. Sci.*, 2022, **15**, 1512–1528.

21 Y. Sun and S. Dai, *Sci. Adv.*, 2021, **7**, 1–24.

22 C. Oses, C. Toher and S. Curtarolo, *Nat. Rev. Mater.*, 2020, **5**, 295–309.

23 T. X. Nguyen, Y. C. Liao, C. C. Lin, Y. H. Su and J. M. Ting, *Adv. Funct. Mater.*, 2021, **31**, 2101632.

24 S. Jiang, T. Hu, J. Gild, N. Zhou, J. Nie, M. Qin, T. Harrington, K. Vecchio and J. Luo, *Scr. Mater.*, 2018, **142**, 116–120.

25 A. J. Wright and J. Luo, *J. Mater. Sci.*, 2020, **55**, 8812–9827.

26 H. Tan, J. Verbeeck, A. Abakumov and G. Van Tendeloo, *Ultramicroscopy*, 2012, **116**, 24–33.

27 D. Qian, B. Xu, M. Chi and Y. S. Meng, *Phys. Chem. Chem. Phys.*, 2014, **16**, 14665–14668.